ACS APPLIED MATERIALS & INTERFACES

www.acsami.org

Research Article

Design and Fabrication of Silicon Nanowire-Based Biosensors with Integration of Critical Factors: Toward Ultrasensitive Specific Detection of Biomolecules

Hui Zhang,* Naoki Kikuchi, Noriyasu Ohshima, Taira Kajisa, Toshiya Sakata, Takashi Izumi, and Hayato Sone

Cite This: *ACS Appl. Mater. Interfaces* 2020, 12, 51808–51819

Read Online

ACCESS | Metrics & More | Article Recommendations | Supporting Information

ABSTRACT: As critical factors affecting the sensing performance of silicon nanowire (SiNW) biosensors, the structure, functional interface, and detection target were analyzed and designed to improve sensing performance. For an improved understanding of the dependence of sensor structure on sensitivity, a simple theoretical analysis was proposed to predict the sensitivity of biosensors with different SiNW types, widths, and doping concentrations. Based on the theoretical analysis, a biosensor integrating optimized critical factors was designed and fabricated. Optimizations focusing on the following aspects are considered: (1) employing n-type SiNW and controlling the impurity doping concentration of SiNW at approximately 2×10^{16}–6×10^{16} atoms/cm^3 to obtain a suitable charge density, (2) minimizing the SiNW width to 16.0 nm to increase the surface area-to-volume ratio, (3) using a native oxide layer on SiNW as a gate insulator to transport the captured charge molecules closer to the SiNW surface, (4) modifying the SiNW surface by 2-aminoethylphosphonic acid coupling to form a high-density self-assembled monolayer for enhancing the stability bound molecules, and (5) functionalizing the SiNW with ovalbumin molecules for specifically capturing the target immunoglobulin G (IgG) molecules. The sensing performance was evaluated by detecting IgG with concentrations ranging from 6 aM to 600 nM and control experiments. The SiNW biosensor revealed ultrahigh sensitivity and specific detection of target IgG with a measured limit of detection of 6 aM. The integration of the critical SiNW biosensor factors provides a significant possibility of a rapid and ultrasensitive diagnosis of diseases at their early stages.

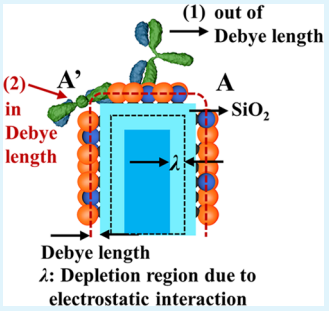

KEYWORDS: *SiNW biosensor, optimization of critical factors, SiNW width, detection limit, ultrasensitive*

1. INTRODUCTION

Rapid, highly sensitive, accurate, and label-free detection of viruses,[1,2] cancer-related biomarkers,[3,4] nucleic acids,[5] cells, and proteins play a critical role in early disease diagnostics.[6,7] However, diseases-related biomolecules exist at very low levels at early stages, such as the viral load of influenza virus A of 3.17 $\log_{10}$ copies/mL[8] and the currently prevalent 2019 novel coronavirus (COVID-19) of under 4 $\log_{10}$ copies/mL,[9] early cancer biomarkers in serum samples are approximately 1−10 ng/mL,[10] etc. Therefore, early disease detection often requires a limit of detection (LOD) in the range of femtomolar (fM) concentrations or lower.[11] For detecting disease-related nucleic acids, real-time polymerase chain reaction (PCR) is widely applied.[12,13] The method has high accuracy but requires expensive equipment, trained professional users, and long detection times, which are not feasible enough to mount a response to control infectious outbreaks. Further, it also yields higher rates of false positives at the early stages of diseases. For fast and affordable detection, rapid visual test products, such as influenza virus antigen detection kits[14,15] and the COVID-19 rapid CE-IVD test kit[16] under development, have the advantages of simplicity, rapid testing, and low cost but are limited by variable detection sensitivity. Thus, there is an urgent need to develop a detection method that can satisfy the requirements of rapid response, high sensitivity, high accuracy, and simple to use for early disease diagnosis.

Silicon nanowire (SiNW) biosensors operate as a field-effect transistors (FETs) and are capable of detecting charged target molecules by monitoring changes in the electrical conductivity of the SiNW channel.[17−19] The sensing capabilities of SiNW biosensors have been demonstrated to include high sensitivity, real-time response, and label-free detection by functionalizing specific recognition elements on the SiNW surface; the LOD, in particular, can be as low as attomolar (aM)−fM concentrations,[20−25] satisfying all of the requirements for early disease diagnosis. In general, the LOD of a SiNW biosensor is highly dependent on three factors: the structure of

Received: August 3, 2020
Accepted: October 21, 2020
Published: November 3, 2020

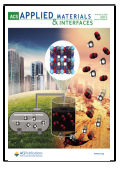

https://dx.doi.org/10.1021/acsami.0c13984
ACS Appl. Mater. Interfaces 2020, 12, 51808–51819

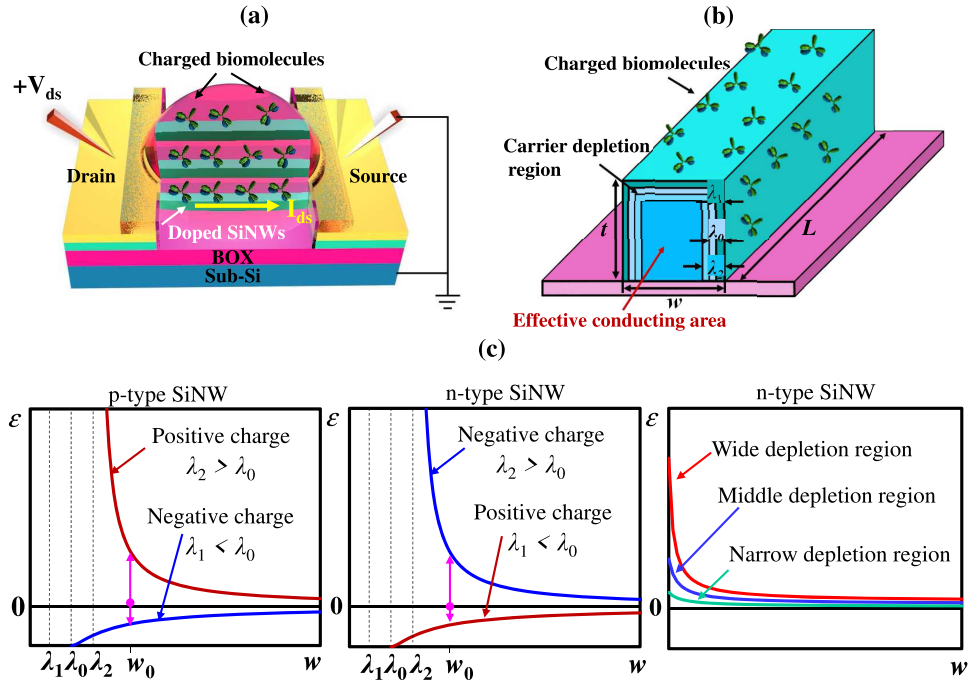

Figure 1. Schematic illustration of the detection mechanism of the SiNW biosensor: (a) detection principle of the silicon nanowire biosensor with molecular gate control, (b) insulation region modulation by charged biomolecule adsorption, (c) dependence of the SiNW type, width, and doping concentration on the resistance change ratio.

the biosensor, the functional SiNW interface, and the detection target.[26,27] The structure of the SiNW biosensor, including the SiNW width, dopant type, dopant concentration, and charge layer distance from the SiNW surface, determines the sensing mechanism of SiNW-FET biosensors. The narrower SiNW and lightly or moderately doped SiNW have been demonstrated to achieve a higher surface-to-volume ratio[28] and enhance the LOD to the aM−fM level.[29] The thickness and shape of the SiNW and arraying of SiNWs also influence the sensing performance of SiNW biosensors but play a relatively minor role in LOD. For the detection of biomolecules with high sensitivity and selectivity, an electrolyte solution/SiNW functional interface such as Debye screening[30] and surface functionalization[31,32] are indispensable for the specific binding of biomolecules to the SiNW surface. The Debye length in physiological solutions is less than 1 nm.[32] To overcome the limitation of the Debye length, functionalizing the surface of SiNWs with small-sized biomolecules, such as aptamers (approximately 2−3 nm) and[33] antigen-binding fragments (Fab, approximately 3−5 nm),[34] has been developed to combine with target molecules within the Debye length. It is possible to increase the Debye length for improved sensitivity by modulating the buffer ionic strength, but it is not possible to dilute buffer solutions in body fluids such as blood, urine, and saliva. In summary, the highest sensitivity of a SiNW biosensor can be achieved when the entire volume of the SiNW is changed by the charged molecules, which requires a good balance between critical factors such as the width, doping, gate insulator thickness on the SiNW surface, and surface modification. However, although very low LODs of aM or sub-10 fM levels have been demonstrated using narrow 20 nm wide SiNWs,[28] as the SiNW dimension is reduced to less than 20 nm, the balance between critical factors becomes much important, but until now, limited studies and experimental data have been published.

In this work, we present a simple theoretical analysis to estimate the dependence of the SiNW type, width, and thickness of the depleted layer of the nanowire (NW) which relates to the doping concentration on the sensitivity of the NW biosensor. Based on the theoretical analysis, a SiNW biosensor integrating optimized critical factors was designed and fabricated by a complementary metal-oxide-semiconductor (CMOS) compatible process. The following fabrication optimizations are considered: (1) employing n-type SiNWs to detect biomolecules with negative charges and controlling the doping concentration to 2×10^{16}−6×10^{16} atoms/cm^3 to obtain suitable charge mobility and density, (2) decreasing the NW width to 16.0 nm to increase the surface area-to-volume ratio, and (3) using a native oxide layer on the NW as a gate insulator to transport the captured charge molecules closer to the NW surface. To evaluate the sensitivity of the optimized biosensor, rabbit anti-ovalbumin immunoglobulin G (IgG) was employed as a model analyte. Target IgG is an antibody with a molecular link connecting the antigen ovalbumin (OVA). To detect target IgG with high sensitivity and specificity, the NW surface functionalization was carefully considered as follows: modifying the surface of the NWs with 2-aminoethylphosphonic acid coupling[35,36] to form a high-density amine-terminated monolayer for enhancing the electrostatic adsorption of recognition molecules and functionalizing the modified NW surface with OVA molecules to capture target IgG molecules. The sensing performance of the NW biosensor integrating critical factors was evaluated by detecting the specific rabbit anti-OVA IgG under various concentrations ranging from 6 aM to 600 nM.

2. EXPERIMENTAL SECTION

2.1. Detection Principle and Design Optimization. Figure 1a shows the conceptual scheme of the proposed SiNW biosensor; it consists of drain and source electrodes and doped NW channels. The

https://dx.doi.org/10.1021/acsami.0c13984
ACS Appl. Mater. Interfaces 2020, 12, 51808−51819

natural growth of the oxide layer on the NW surface is employed as the gate dielectric. The working principle of the biosensor is similar to a solution-gate FET.[37] The source is grounded, whereas a positive bias is applied to the drain, resulting in a drain−source voltage (V_{ds}). The charged molecules are employed as a gate (V_g) to adjust the charge carrier density of the SiNWs. The back-gate contact is grounded and has the same potential as the source contact. The drain−source current (I_{ds}) that flows through the SiNWs from the drain to the source is measured in this work to detect target molecules at different concentrations. In the case of an n-type NW, the measured current will decrease with the accumulation of negatively charged biomolecules on the functionalized NW surface. Conversely, for a p-type NW, the current will increase and the resistance of the NW will decrease. Here, it should be noted that the doping concentrations were the same in the SiNW channel and contact regions, which results in the SiNW channel being in the "ON" state without external gate voltage control. Because of this, the charge density of the doped SiNW channel can be altered by a small electric charge, and thereby, it is possible to detect biomolecules at an extremely low concentration.

In addition, for a theoretical study on biosensor sensitivity, a simple theoretical model of the SiNW was proposed. We model the nanowire as a rectangular cuboid with a width w, a thickness t, and a length L, as shown in Figure 1b. The top surface and the other two surfaces of SiNW are available for the binding of biomolecules. For an n-type SiNW biosensor, the thickness of the carrier depletion region is λ_0, which is governed by the Si/SiO_2 interface trap density and dopant/carrier concentration.[38] Therefore, the initial resistance R_0 is given as

$$R_0 = \rho \frac{L}{(w - 2\lambda_0)(t - \lambda_0)} \quad (1)$$

where ρ is the resistivity of SiNW, which is adjusted by controlling the number of dopant atoms per unit volume.

When negatively charged biomolecules bind to the surface of SiNW, this leads to a decrease of charge carriers in the sensing area due to electrostatic repulsion, and the thickness of the depletion region increases from λ_0 to λ_2. Conversely, positively charged biomolecules would render an increase in charge carriers of the sensing channel, and the thickness of the depletion region would decrease from λ_0 to λ_1. Here, using λ instead of λ_1 and λ_2 as the thickness of the depletion region, the resistance of SiNW after biomolecule binding can be written as

$$R = \rho = \frac{L}{(w - 2\lambda)(t - \lambda)} \quad (2)$$

On the basis of the above analysis, the resistance change ratio (ε) of SiNW before and after biomolecule binding can be given as

$$\varepsilon = \frac{\Delta R}{R_0} = \frac{\{w + 2t - 2(\lambda + \lambda_0)\}(\lambda - \lambda_0)}{(w - 2\lambda)(t - \lambda)} \quad (3)$$

The above mechanism can also be extended to the behavior of p-type SiNWs. Therefore, the dependence of the SiNW type and width on the resistance change ratio by varying the width of the SiNW (w) and the thickness of the depletion layer (λ_0 and λ) can be obtained, as shown in Figure 1c. It can easily be concluded that for SiNW of the same width (w_0), the resistance change ratio of n-type SiNW is more sensitive to negatively charged molecules than that of p-type SiNW. Moreover, decreasing the width of SiNW is beneficial to increasing the sensitivity. From the relationship between the depletion region width and resistance change ratio, we can see that as the depletion region becomes wider, the resistance change ratio increases. As is well known, the depletion region width is related to the doping concentration; therefore, lower doping could increase the sensitivity. In this work, the target IgG molecule carries a negative charge. Based on this theoretical analysis, an n-type SiNW biosensor with a NW width of less than 20 nm and light doping concentration was determined to increase sensitivity. Furthermore, in general, increasing the NW length increases the number of biomolecules that can bind to the NW; however, an increase in the NW length also increases the internal electrical resistance and may compromise the electrical characteristics of the NW, especially in the cases of narrow width and light doping concentration. Since the length term of the NW cancels out in eq 3, SiNWs with a relatively short length of 14 μm were adopted, and NW arrays were employed to ensure reliability and reproducibility.

In addition to these physical factors, the performance of the SiNW biosensor is also influenced by surface functionalization. Therefore, we also proposed an effective surface functionalization method to improve the sensitivity of the biosensor.

2.2. SiNW Biosensor Fabrication. A schematic diagram of the SiNW biosensor fabrication process is shown in Figure 2. A

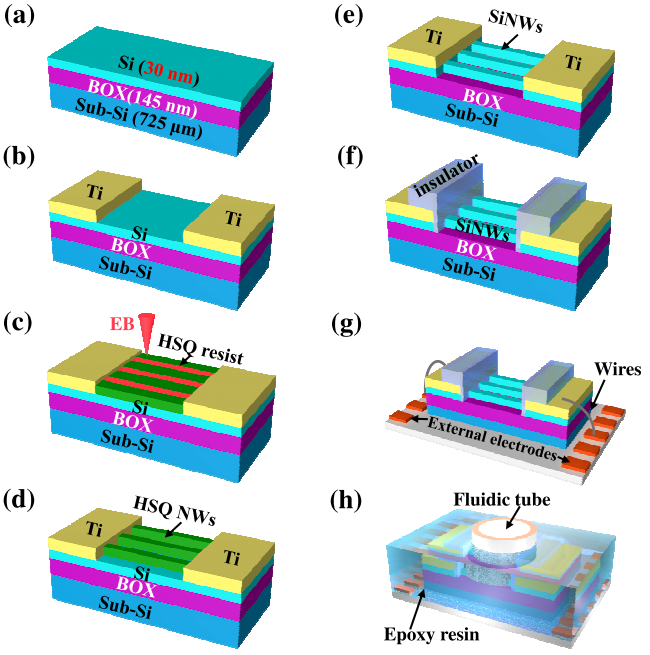

Figure 2. Schematic illustration of the SiNW biosensor fabrication process: (a) thinning the top Si layer by ICP-RIE and phosphorus doping by thermal diffusion; (b) fabricating Ti electrodes with a gap of 14 μm by photolithography, sputtering, and liftoff processes; (c) spin-coating HSQ resist on the SOI wafer; (d) fabricating HSQ nanowires in the gap between electrodes by EB writing; (e) transferring HSQ nanowires into a Si layer by ICP-RIE; (f) forming an isolation layer on the surface of electrodes; (g) connecting electrodes of the biosensor to the external electrodes by wire bonding; and (h) integrating the biosensor with a PTFE tube microfluidic channel and a packaging biosensor with epoxy resin.

commercial silicon-on-insulator (SOI) wafer was used as a substrate. The SOI wafer consists of a 70 nm thick ⟨100⟩ oriented top silicon layer, a 145 nm thick buried oxide (BOX) layer, and a 725 μm thick silicon substrate. Both the top and substrate silicon layers are p-type boron-doped Si, with a resistivity of 9−18 Ω·cm. To obtain a narrow conducting channel with high sensitivity to biomolecules, the 70 nm top Si layer was thinned to 30 nm by inductively coupled plasma reactive ion etching (ICP-RIE, CE300I, ULVAC). Before device fabrication, contaminants and the native oxide layer of the SOI wafer were removed by an organic solvent (acetone and ethanol) and 10% hydrofluoric acid (HF) solution, respectively. Next, to form an n-type Si layer, a thermal diffusion process with a dopant solution including P_2O_5 (OCD T-1 P-59230, Tokyo Ohka) was adopted. It is worth noting that the phosphorus dopant thickness and the temperature of thermal diffusion were controlled to achieve a low doping concentration of phosphorus of approximately 2×10^{16}−6×10^{16} atoms/cm^3, which is particularly important for the sensitive detection of negatively charged biomolecules.[39] After thermal diffusion, the oxide layer of the SOI wafer was removed using a 15% buffered hydrofluoric (BHF) acid solution. Subsequently, 65 nm thick titanium

https://dx.doi.org/10.1021/acsami.0c13984
ACS Appl. Mater. Interfaces 2020, 12, 51808−51819

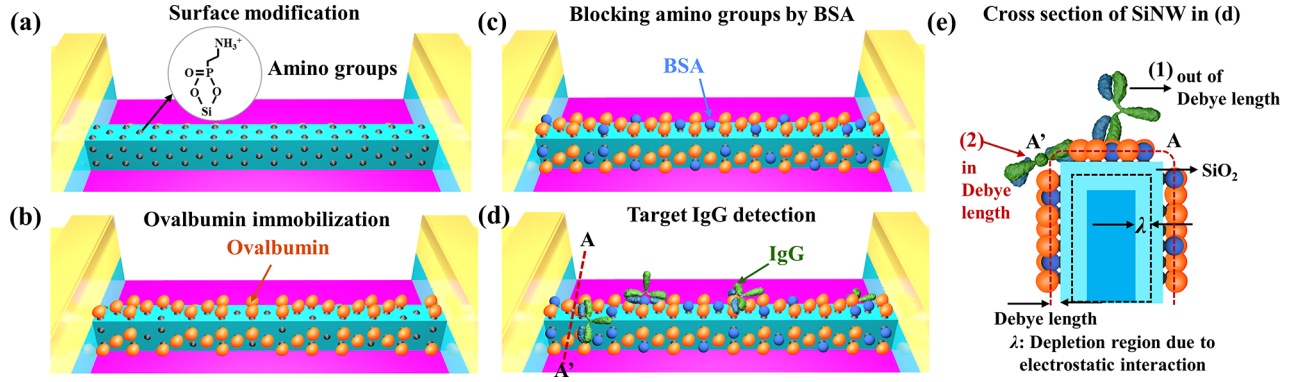

Figure 3. Schematic illustration of the surface functionalization of SiNWs: (a) surface modification by dilute hydrochloric acid with a concentration of 1 M and 2-aminoethylphosphonic acid coupling, (b) antigen immobilization by OVA, (c) blocking unreacted amino groups by bovine serum albumin (BSA), and (d) detection of target IgG. (e) Cross section of SiNW in (d), with the cases of IgG binding with OVA in and out of the Debye length.

(Ti) electrodes were patterned onto the SOI wafer using conventional photolithography (Photomask aligner PEM-800, Union Optical Co.) to transfer the electrode pattern and deposited by sputtering (MNS-3000-RF) and a liftoff process (Figure 2b). Nanowires were fabricated on the prepared substrate by direct-write electron beam (EB) writing (Figure 2c,d). The EB writing system is a combination of a high-resolution scanning electron microscope (SEM) with a Schottky emission-type field-emission electron gun (JSM6500F, JEOL) and a drawing controller (Beam Draw, Tokyo Technology).[40] To form narrow nanowires with high-resolution, negative-tone resist hydrogen silsesquioxane (HSQ, Dow Corning) and a high-contrast salty development solution[41,42] were employed. Normally, a thin HSQ resist layer would be employed to form a high-resolution pattern because the EB scattering range (lateral) in a thin resist layer is smaller than that in a thick resist layer. However, as the HSQ resist layer becomes thinner, transferring HSQ nanowire patterns to the Si layer becomes difficult due to the low etching selectivity of HSQ and Si. Here, the thickness of the HSQ resist was controlled at 37 nm using 6 wt % HSQ diluted in a methyl isobutyl ketone solution. Nanowires of design width 10 nm, pitch 300 nm, and length 25 μm were written by EB writing using a probe with a diameter of <2 nm and a probe current of 200 pA at an accelerating voltage of 30 kV. The optimal exposure dosage was investigated by varying the exposure dosage from 40 to 60 mC/cm^2, and the surface morphology of the NWs was evaluated by SEM investigation. After HSQ nanowire fabrication, ICP-RIE (CE300I, ULVAC) was applied to form SiNWs using CF_4 plasma etching (Figure 2e). As the HSQ nanowires become narrower, they become too weak for aggressive plasma etching; therefore, the plasma etching conditions should be precisely controlled. CF_4-RIE was performed at a radio frequency (RF) power of 60 W, a gas flow rate of 5 sccm, and an RF bias power of 5 W to maintain an HSQ resist etching rate under 0.25 nm/s. Moreover, to decrease the contact resistance between the Ti electrodes and SiNWs, an annealing process was performed at 400 °C for 30 min in an Ar environment. Next, a SU-8 (MicroChem) isolation layer with a thickness of 5 μm was fabricated by photolithography with position alignment to prevent current leakage from the electrodes and form an open fluidic channel for biomolecule sensing (Figure 2f). Then, the SOI wafer was diced into separate devices by stealth laser dicing (DFL7340). To measure the electronic characteristic of each device, wire bonding (7476D, West Bond) of the exposed Ti electrode to an external copper (Cu) electrode was performed (Figure 2g). Finally, a poly(tetrafluoroethylene) (PTFE) tube with an inside diameter of 2 mm was placed in the sensing area of the device to form an open fluidic channel for sensing, and the whole device was packaged with epoxy resin,[43] as shown in Figure 2h. The volume of the sensor tube is 10 μL; thus, protein solutions with the same volume were used in the work.

2.3. Experiments for Specific Biomolecule Detection. For identifying specific biomolecules, functionalization of the SiNW surface and an immobilization mechanism are crucial and require careful considerations. We employed 2-aminoethylphosphonic acid coupling[35,36] instead of the conventional surface modification method using 3-aminopropyl triethoxysilane (APTES) to form a dense amine-functionalized self-assembled monolayer (SAM) on the SiNW surface, as shown in Figure 3a. The advantages of aminoethylphosphonic acid coupling in forming SAM with a more stable and higher density than using APTES are demonstrated. The reason is that silanization just consumes surface OH groups to form siloxane linkage (Si−O−Si) with organic silane molecules; in contrast to silanization, the phosphonate methodology uses OH groups as catalysts for comprehensive surface coverage.[44] The surface modification process began by immersing the SiNW biosensor in dilute hydrochloric acid at a concentration of 1 M for 30 min. At this time, the native oxide layer covalently bonded with hydroxyl groups (OH^-) to form silanol groups (SiOH). Next, the sample was immersed in 2-amino-ethylphosphonic acid (Wako) coupling solution at a concentration of 1 mM, which was dissolved in deionized (DI) water for 24 h at room temperature. The solvent was allowed to evaporate slowly so that the meniscus slowly traversed the surface of the coupon, transferring phosphonic acid to SiO_2/Si.[45] Then, the sample was heated in a vacuum oven at 140 °C for 48 h and finally rinsed by sonication with isopropyl alcohol 2-propanol (IPA) for 3 min to remove any unreacted aminoethylphosphonic acid coupling.

The detection target, rabbit anti-OVA IgG (CEDARLANE, CLAG8140), is a polyclonal antibody and is shipped at an initial concentration of 9.0 mg/mL in a phosphate-buffered saline (PBS) solution. The molecular mass of IgG is approximately 150 kDa, with dimensions of 13.7 nm (width) and 8.4 nm (height).[46] To detect target IgG, the antigen OVA (albumin from chicken egg white, Wako, 016-17073) was employed to functionalize the SiNWs. The molecular mass of OVA is approximately 45 kDa with a radius of approximately 3 nm.[47] Here, a PBS solution with a pH of 7.4 was used for dilution of proteins throughout the work to ensure that the antigen and antibody solutions have equal salt concentrations and pH values, ensuring that any change in the current signal is due to the specific binding of the antigen and antibody. The PBS solution consists of 137 mM sodium chloride (NaCl), 2.7 mM potassium chloride (KCl), 8 mM sodium hydrogen phosphate (Na_2HPO_4), and 1.5 mM potassium dihydrogenphosphate (KH_2PO_4). In general, for detecting specific antibody−antigen binding, antibodies were immobilized on SiNWs for specific antigen capture. However, the Debye length in this PBS salt environment is approximately 1 nm;[30] thus, if we immobilized the target IgG antibody onto SiNW for capturing specific OVA, part of the IgG antibody molecules may remain outside the charge-detectable region, resulting in no response to OVA−IgG binding. Therefore, OVA antigen-immobilizing molecules with small sizes were selected for the detection of specific IgG antibody, as shown in the schematic illustration in Figure 3b. To eliminate the nonspecific binding, bovine serum albumin (BSA) was used for blocking the SiNW surface. As

https://dx.doi.org/10.1021/acsami.0c13984
ACS Appl. Mater. Interfaces 2020, 12, 51808−51819

shown in Figure 3c. Afterward, IgG biomolecules were introduced to the sensing area to bind with OVA, as shown in Figure 3d. Considering overall groups of amino linkers and OVA, although the binding of IgG seems to exceed the Debye length, in general, only a small part of antigen, known as the epitope, can be recognized by a specific antibody. An epitope is small, just approximately 4−10 amino acids in length. The position of the epitope on the antigen or random orientation of antigen biomolecules to the SiNW surface can result in the occurrence of some antigen−antibody binding within the Debye length.[48] In the side view of the schematic illustration, as shown in Figure 3e, in the case of the IgG molecule of (1), it was bound to the epitope that was located on the upside of OVA. Then, the IgG molecule was outside the Debye length, so that it cannot be detected due to the electrostatic shield. For the IgG molecule of (2), it was bound to the epitope located on the side of the OVA at the SiNW edge. Then, a part of IgG was in the Debye length; therefore, the electrical charges within the Debye length can be detected by the ultrasensitive biosensor. This is exactly our purpose of the work, i.e., to design and fabricate SiNW biosensors with the integration of critical factors for ultrasensitive detection.

For functionalizing SiNW with OVA, OVA with a high concentration of 10 μM (diluted in PBS) and immobilized for 15 min was adopted to obtain a suitable surface receptor coverage.[49] The concentration of OVA to be used was determined through an antigen saturation study, which was performed in a separate experiment. After that, the OVA solution was removed from the sensor tube to finish SiNW functionalization. Next, a high concentration (10 μM) of BSA (molecular mass of approximately 66 kDa, Wako, 016-15091) was used to block the nonspecific protein interactions of the biosensor for 15 min. After the blocking process, the SiNW biosensor was ready for the detection of target IgG. To estimate the sensitivity of the SiNW biosensor, IgG solutions with concentrations from 6 aM to 600 nM were prepared by serially diluting the initial IgG solution in PBS. After the addition of the target IgG solution, the sensor was incubated for 15 min to allow sufficient time for binding of target IgG with surface-functionalized OVA.

To verify the specificity of the biosensor, two control experiments were conducted. One control experiment was performed before the target IgG detection by normal rabbit serum IgG (cIgG, molecular mass of approximately 150 kDa, Sigma-Aldrich, I8140) as a control antibody. The concentration of cIgG was 7.6 μM (diluted in PBS). For the second control experiment, we used BSA protein instead of OVA to functionalize the NW surface and then introduced target IgG to the BSA-functionalized SiNW surface to investigate whether the current through the SiNWs changed. The real-time current measurement was performed during OVA functionalization, BSA blocking, target IgG detection, and the control experiments to validate the binding. After one assay step, the current measurement was paused before the protein solution exchange and then restarted after the addition of the protein solution.

3. RESULTS AND DISCUSSION

3.1. SiNW Fabrication and Electrical Characteristics of the SiNW Biosensor. Figure 4a shows the biosensor chip with dimensions of 2 × 2 cm^2 and contains 24 biosensors. Enlarging the gap between the electrodes, we can see that the HSQ nanowires were placed at the predetermined locations connecting the source and drain electrodes, as shown in Figure 4b. Each biosensor has an array of 20 nanowires with a lateral pitch of 250 nm. Although employing nanowire arrays cannot increase sensitivity directly, it can ensure device stability and reliability and decrease device resistance. Figure 4c,d shows the SEM images of HSQ NWs with a width of 26.9 nm and a length of 25 μm at an exposure dosage of 52 mC/cm^2 and SiNWs with a width of 16 nm and a length of 14 μm after CF_4 plasma etching for 120 s, respectively. Compared with the widths of NWs before and after etching, it can be seen that the width of the nanowires was reduced by approximately 10 nm.

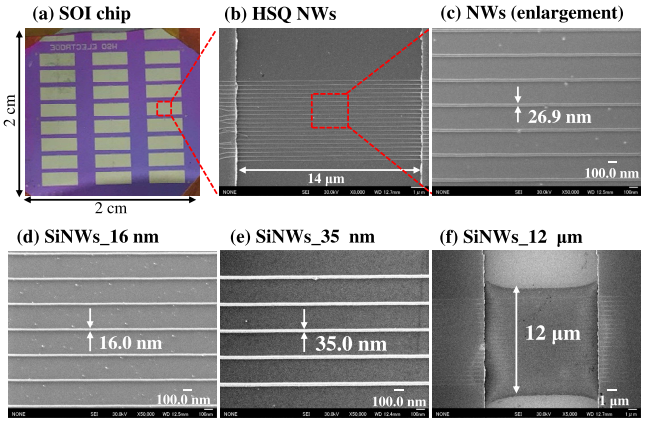

Figure 4. (a) Overall image of SOI chip that contains 24 biosensors, (b) SEM images of HSQ nanowires between the gap formed by the Ti electrodes, (c) SEM image of HSQ nanowires with a width of 26.9 nm and a length of 25 μm, formed at an exposure dosage of 52 mC/cm^2, (d) SEM images of SiNWs with a width of 16.0 nm and a length of 14 μm, which was formed by transferring the HSQ NWs shown in (c) to the Si layer with CF_4-RIE, and (e, f) SEM images of SiNWs with a width of 35 nm and 12 μm, respectively. The SiNWs of 16 nm, 35 nm, and 12 μm were formed on the same SOI chip that has the same thickness and doping concentration.

Moreover, the HSQ NWs with the length of 25 μm formed on the Si layer and overlap the electrodes, as shown in Figure 4b. As the electrodes were nearly unetched by CF_4 plasma, the NWs were transferred to the Si layer. Therefore, the length of SiNWs was 14 μm as large as the gap between electrodes. For investigating the impact of SiNW width on the sensing capability, SiNWs with different widths of 35 nm and 12 μm were fabricated, as shown in Figure 4e,f.

In addition, the topography of 16 nm wide SiNWs was evaluated by atomic force microscopy (AFM; WA-200, Hitachi), as shown in Figure 5a−c, and the average height was measured as 23.3 nm. From the AFM results, it can be seen that the bottom width of SiNWs is wider than its top width due to the limitations of the cantilever (OMCL-TR800PB-1, OLYMPUS) tip geometry. The average bottom width was approximately 64 nm, and the tip diameter of the cantilever was estimated to be 48 nm. Here, the shape of the cantilever was investigated by SEM (S-900, Hitachi) with a high resolution of 1 nm, as shown in Figure 5d. As the AFM image and line profile represent the convolution of the tip diameter with the NW, the average width of SiNWs was estimated as 16 nm. This value agrees with the value measured by the SEM observation. The results indicate that the SiNWs were formed with low edge roughness, high resolution, and good pattern placement.

To confirm that the current of SiNWs can be modulated effectively by the potential of gate voltage, the FET characteristics of 16 nm, 35 nm, and 12 μm wide SiNWs were measured, respectively, using a sub-femtoamp source meter (2636B, Keithley). A direct current (DC) voltage between the drain and source electrodes was swept from −0.1 to 0.1 V with an increment of 5 mV. Ten microliters of PBS solution was injected into the tube as a medium and an AgCl reference electrode was immersed into the PBS solution and used to apply the top-gate voltage V_g, as shown in the inset of Figure 6a. The source−drain current−voltage I_{ds}−V_{ds} dependence of V_g varied from 0 to 1 V in increments of 0.2 V; the I_{ds}−V_g and leakage current I_g−V_g for V_{ds} = 0.1 V of SiNWs with

https://dx.doi.org/10.1021/acsami.0c13984
ACS Appl. Mater. Interfaces 2020, 12, 51808−51819

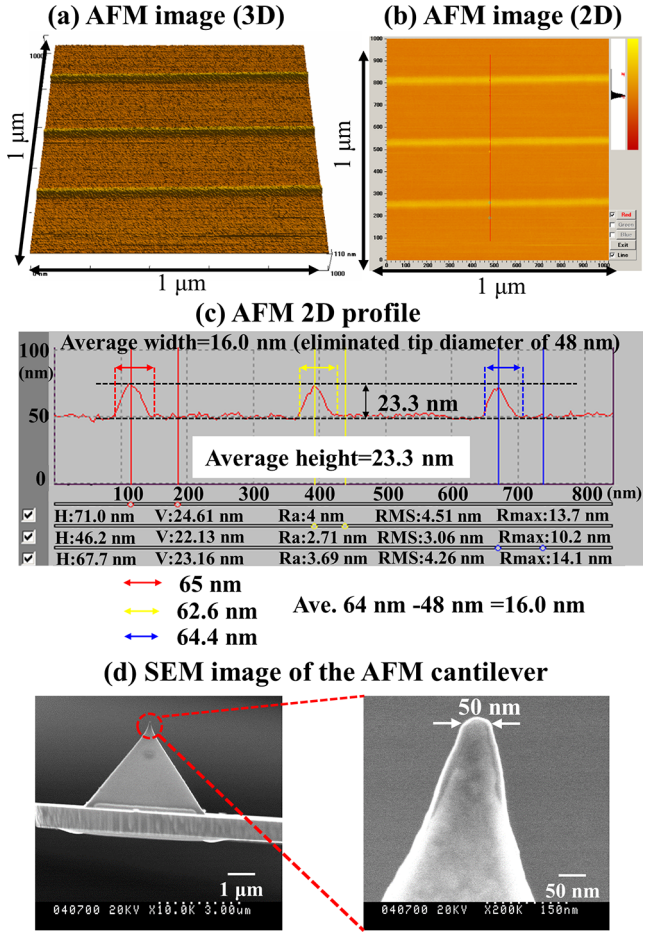

Figure 5. (a, b) AFM images of SiNWs in both three dimensions (3D) and two dimensions (2D), (c) height profile of fabricated SiNWs, and (d) SEM observation image of the AFM cantilever.

widths of 16 nm, 35 nm, and 12 μm are shown in Figures 6, S1, and S2, respectively. Figures S1 and S2 are in the Supporting Information. From the I_{ds}–V_{ds} curves, it can be clearly seen that the drain current increased in all the SiNW biosensors when a positive voltage was applied, which is in agreement with the performance characteristic of an n-type FET device. As observed from the I_{ds}–V_g transfer behavior, the electron carriers passing through the SiNW channels from the source to the drain could be efficiently modulated by the gate voltage. From the curve of I_g responses to V_g of SiNWs with different widths, it can be seen that all of the leakage currents were much lower than I_{ds}, which can be ignored. It was verified that the dielectric properties of the native oxide layer were stable enough to avoid any current leakage from the NW into the liquid. For further confirmation of the nanoscale effect on FET characteristics, the current change ratio responses to gate voltage under SiNWs with different widths were compared, as shown in Figure 7. The source–drain current at V_g = 0 V was

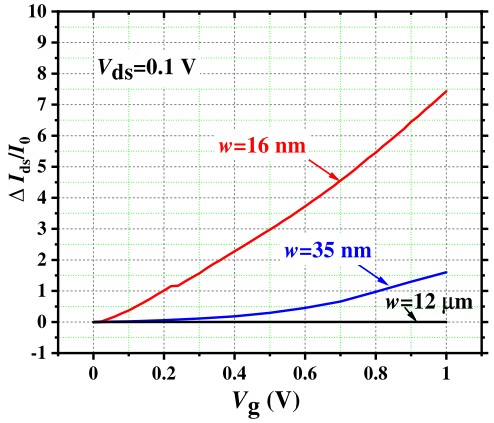

Figure 7. Comparison of current change ratios versus V_g using SiNWs with different widths.

defined as I_0, the gate voltage applied onto the NWs produced a change in current $(I_{ds} - I_0)$, and the current change ratio was calculated by $(I_{ds} - I_0)/I_0$. It can be clearly seen that the current change ratio drastically increases as the width of SiNW decreases. Although there was no significant width difference between 16 and 35 nm, the current change ratio showed a difference of 20 times at even a low gate voltage of 0.1 V. The SiNW with a width of 12 μm, similar to that of a planer FET device, is insensitive to the gate voltage. It can be considered that when an additional V_g was applied to the interface of the SiNW channel and solution, the electric field produced in the channel drives the change in the depletion region. As the SiNW becomes narrower, the ratio of the change of the depletion region to the whole channel becomes higher, which

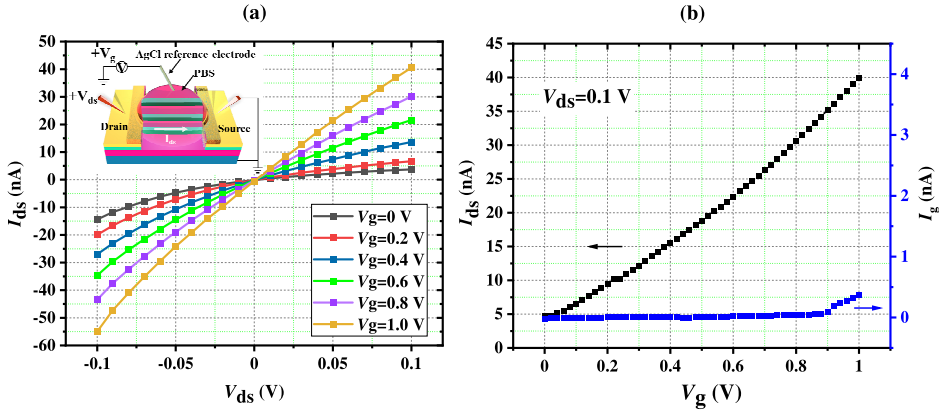

Figure 6. (a) I_{ds}–V_{ds} curve for V_g varied from 0 to 1 V, illustrating n-type accumulation mode behavior. Inset: schematic diagram of the measurement system for evaluating the FET performance. (b) I_{ds}–V_g transfer characteristic and I_g–V_g curve of the SiNW biosensor for a constant V_d at 0.1 V.

https://dx.doi.org/10.1021/acsami.0c13984
ACS Appl. Mater. Interfaces 2020, 12, 51808–51819

is the reason why the current of the narrow SiNW channel can be modulated more efficiently by a low gate potential. The measurement results were in agreement with the predicted results based on the previously presented theoretical model. As a result, the biosensor with a SiNW width of 16 nm displaying superior FET characteristics was adopted for target IgG detection.

3.2. Detection Performance of the SiNW Biosensor. The real-time response of currents through the SiNWs during OVA immobilization, BSA blocking, control experiments, and target IgG detection were monitored to gain a better understanding of the sensor performance. Here, a constant voltage of 0.1 V was applied to the source and drain. The back-gate contact was grounded and therefore fixed to the same potential as the source contact. The charges of the protein act as the top-gate to modulate the current of SiNW. Figure 8a shows the real-time current response upon the injection of various protein solutions over 15 min. The average current of the last 60 s was used to calculate I_{ds}. The I_{ds} in the PBS solution was stable at approximately 21.2 nA, establishing the baseline current relative to which changes in the current were measured. During OVA immobilization, the OVA molecules bind to the amine-modified SiNWs by electrostatic absorption while introducing additional negative charges to the solid (SiNW surface)−liquid (OVA solution) interface. Therefore, a decrease in the I_{ds} of the SiNWs upon immobilization of OVA is observed. Here, the current decreased continuously and the decrease in current with respect to the baseline PBS measurement was approximately 0.9 nA. To avoid nonspecific binding of target IgG, a molecular blocking layer of BSA was used. BSA was applied to the whole sensor surface to block the nonfunctionalized surface of OVA immobilization. After BSA blocking, the current decreased approximately 1.0 nA with respect to the I_{ds} of OVA immobilization, demonstrating that the nonfunctionalized surface was blocked by BSA due to nonspecific binding. It can also be estimated that the surface receptor OVA coverage did not achieve full saturation. After blocking, the sensor was ready to detect target IgG.

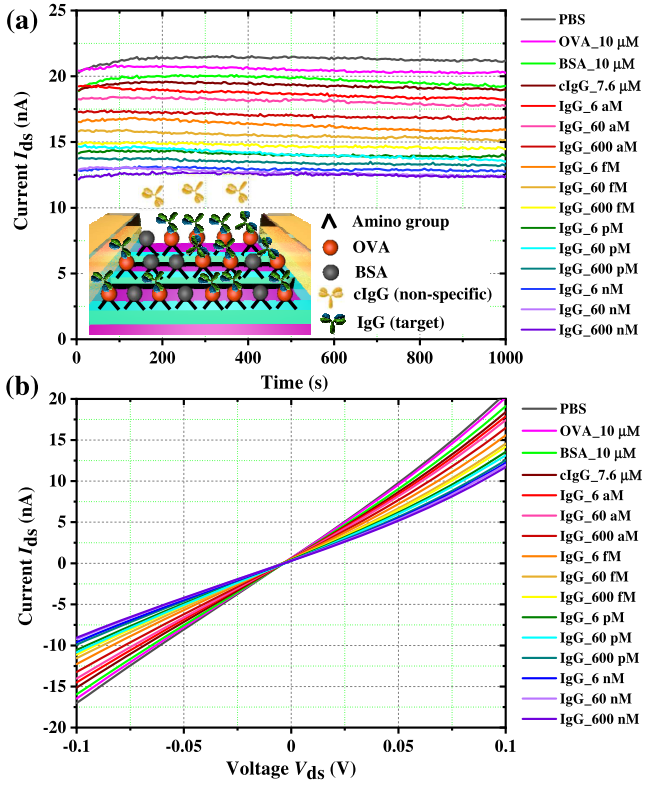

Figure 8. (a) Real-time current measurement of the biosensor with 16 nm SiNWs during the processes of antigen immobilization, blocking nonspecific binding sites, and control experiments with nonspecific antibody and specific antibody detection. The conceptual diagram of these processes is shown in the inset. (b) $I-V$ electrical characteristics of the SiNW biosensor to various biological solutions.

As introduced in the previous section, a control experiment with the cIgG protein was performed prior to target IgG detection. The current response to the cIgG protein shows that although cIgG with a high concentration was introduced to the SiNW surface, it did not lead to a significant current change. The current decreased just 0.25 nA compared to the BSA-blocking step, indicating that the cIgG protein did not bind to OVA or BSA and also demonstrating that no nonspecific binding had occurred because the SiNW surface-functionalized sites were saturated. To demonstrate the sensitivity and LOD of the SiNW biosensor, the current response to different concentrations of target IgG, ranging from 6 aM to 600 nM, was investigated in order after the control experiment. The I_{ds} of cIgG was used as the reference current to calculate the current change for various concentrations of target IgG. By adding a 6 aM IgG solution, a sufficient decrease in the electrical current of approximately 0.72 nA was obtained. The concentration of the IgG solution was 10^{12}-fold lower than that of nonspecific cIgG, but the current change was almost three times higher than that of cIgG. It is clear that the current change was observed by the specific binding of OVA−IgG. Moreover, the addition of target IgG with concentrations of 60 aM, 6 fM, 600 fM, 60 pM, 6 nM, and 600 nM resulted in continuous decreases in I_{ds} of 1.22, 3.14, 4.50, 5.40, 6.21, and 6.64 nA, respectively. It can be concluded that the negative charges accumulate on the surface of SiNWs as the OVA−IgG binding-induced concentration increase occurs, resulting in a decrease in current through the SiNWs. As observed from Figure 8a, it can be seen that when the concentration exceeds 60 nM, the changes of I_{ds} over time became smaller compared to other concentrations. It can be considered that the OVA−IgG binding was saturated at a concentration of 60 nM.

To investigate resistance change ratios for different biological solutions, the $I-V$ characteristics for a direct current−voltage of −0.1 to 0.1 V in increments of 5 mV were each measured three times in real-time. Figure 8b shows the average $I-V$ of the SiNWs response to different biological solutions. It can be clearly seen that the slope of the $I-V$ characteristics decreases as the target IgG concentration increases, which agrees with the current change trend of Figure 8a.

For further evaluation of the device performance, the resistance change ratio of the SiNW biosensor as a function of the target IgG concentration was calculated based on the average $I-V$ characteristics. The average resistance of SiNWs in the cIgG solution was considered as the reference value R_0. The average resistance in the target IgG solution is denoted R. The relative resistance change ratio can be calculated as $(R - R_0)/R_0$. Figure 9 shows the logarithmic IgG concentration dependence of resistance change ratios and current change ratios. The error bars were calculated based on the $I-V$ characteristics, which were measured three times. In an ultralow concentration of 6 aM IgG in the PBS solution, a resistance change ratio of approximately 5% was obtained. The

https://dx.doi.org/10.1021/acsami.0c13984
ACS Appl. Mater. Interfaces 2020, 12, 51808−51819

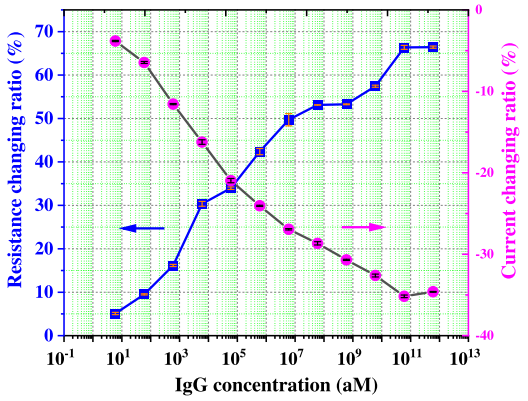

Figure 9. Resistance change ratios and current change ratios of the SiNW biosensor response to target IgG with different concentrations.

resistance change ratio increases with the logarithmic concentrations of IgG from 6 aM to 600 nM. When the IgG concentration was increased to 60 nM, the resistance change ratio increased more slowly because the IgG molecules bound to the OVA became saturated. On the basis of the above analysis, it can be concluded that the SiNW biosensor detected IgG biomolecules at the ultralow concentration of 6 aM. The number of IgG molecules in 10 μL with a concentration of 6 aM is approximately 36.

To further demonstrate the specificity of the SiNW biosensor, a second control experiment of functionalizing SiNW with BSA was performed as a separate experiment, and the resulting resistance change ratio responses to target IgG with various concentrations are shown in Figure 10a. Here, the

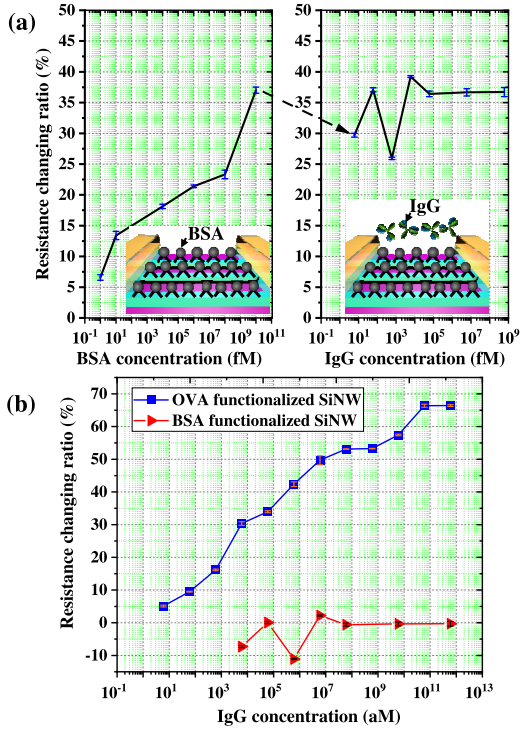

Figure 10. Results of control experiments. (a) Resistance change ratio response to various concentrations of IgG of BSA-functionalized SiNW biosensor. (b) Comparison of resistance change ratio dependence of IgG concentration based on both OVA-functionalized SiNWs and BSA-functionalized SiNWs.

width of the SiNWs was 20 nm. First, the BSA solution was introduced into the sensor tube in sequence from a low concentration of 1 fM to a high concentration of 10 μM with incubation times of 15 min for each solution. The purpose of this step was to saturate the SiNW surface with the BSA protein to prevent nonspecific binding. From the resistance change ratio dependence of the BSA concentration, it is clear that as the BSA protein binds to the SiNW surface, the resistance of SiNWs increases continuously. After the SiNW surface is saturated with BSA, PBS solutions with target IgG with concentrations ranging from 6 fM to 600 nM were introduced to the SiNW surface. As can be seen, the control signals fluctuated at low concentrations of IgG but became stable at higher concentrations. The resistance change ratio did not show any significant increase in either low or high concentration of target IgG. Figure 10b summarizes the resistance change ratio dependence of IgG concentration based on both OVA-functionalized SiNWs and BSA-functionalized SiNWs. A clear and significant increase in the resistance change ratio as the IgG concentration increases was obtained in the OVA-functionalized SiNW biosensor. It was demonstrated that the electrical signal change was derived from the specific binding of IgG−OVA and the SiNW biosensor was highly specific.

3.3. Estimation of Dissociation Constant. To understand the binding kinetics of target IgG and OVA, the dissociation constant (K_d) was estimated from the current change (ΔI_d) as a function of the target IgG concentration. To calculate ΔI_d, the average current of the last 60 s of the real-time current measurement was adopted. The average current of the biosensor in the cIgG solution was considered as the reference value I_0, the average current of the biosensor in albumin solution as I, and ΔI_d was calculated as $I - I_0$. Figure 11 shows the current change ($-\Delta I_d$) of the SiNW biosensor as

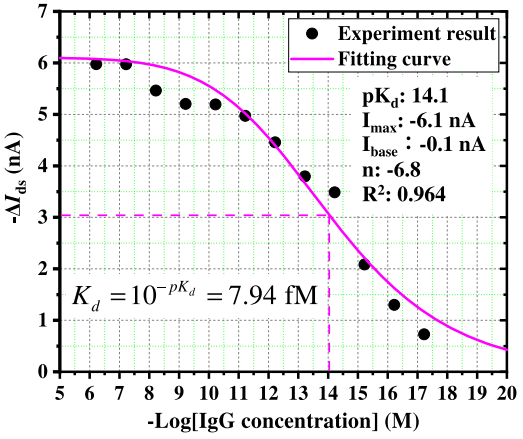

Figure 11. Current change as a function of the logarithmic target IgG concentration, which was fitted to a Hill adsorption isotherm (lines) to investigate the dissociation constant between OVA and target IgG.

a function of the logarithmic IgG concentration. The value of $-\Delta I_d$ sharply increased with increasing IgG concentration from 6 aM to 600 nM and then gradually saturated after 60 nM. A nonlinear curve was successfully fitted by a sigmoidal function based on the Hill absorption equation.[50,51]

$$\Delta I = \Delta I_{max} - (\Delta I_{max} + \Delta I_{base}) / \left(1 + \left(\frac{pC_{IgG}}{pK_d}\right)^n\right) \quad (4)$$

https://dx.doi.org/10.1021/acsami.0c13984
ACS Appl. Mater. Interfaces 2020, 12, 51808−51819

Table 1. Comparison of the Sensing Performance of the Improved Biosensor with Other SiNW Biosensors Based on Antibody and Antigen Binding

device specification	width (nm)	doping concentration (cm^{-3})	target analytes	LOD	reference
p-type SiNWs	50	10^{15}	insulin	10 fM	53
p-type SiNWs	200	10^{16}–10^{17}	antigen	5 fM	54
n-type SiNWs	20		carcinoembryonic antigen (CEA)	0.55 fM	55
n-type SiNWs	90	3×10^{18}	PSA	30 aM	29
n-type SiNWs	16	2×10^{16}–6×10^{16}	IgG	6 aM	this work

where ΔI_{max} and ΔI_{base} are the approximate maximum and minimum ΔI, respectively, pK_d is the logarithmic dissociation constant of the specific binding between OVA and target IgG, which is equal to $-\log_{10}(K_d)$, pC_{IgG} is the logarithmic IgG concentration, and n is the Hill coefficient. Based on the least-squares method, ΔI_{max}, ΔI_{base}, pK_d, and n were estimated to be −6.1 nA, −0.1 nA, 14.1, and −6.8, respectively. The correlation coefficient R^2 was 0.964 in the experimental results fitting, which can be used to determine the best fitting isotherm to the experimental data. Based on the analysis, the dissociation constant K_d was calculated as 7.9 fM. The dissociation constant K_d between OVA and monoclonal antibodies has been detected by surface plasmon resonance and determined to be approximately 2.4×10^{-8}–3.1×10^{-8} M.[52] Here, the dissociation constant evaluated from experimental data was approximately 6 orders of magnitude lower than the reported K_d value. The following three aspects should be considered to understand this: (1) the integration of critical factors on SiNW biosensor greatly improves the detection capability for low electrical potential of biomolecules, which was also demonstrated by the FET characteristics. The details of specific impacts can be considered as employing n-type SiNWs is beneficial to detecting negatively charged molecules; scaling down the SiNW width and decreasing the doping concentration can increase the proportion of the depletion region thickness over the whole SiNW width. (2) The surface functionalization of SiNWs improves the binding of OVA–IgG for the following reasons: modifying SiNW with 2-aminoethylphosphonic acid coupling provided a high-density SAM layer to ensure increased stability of OVA immobilization. (3) As we introduced in the previous section, target IgG is a polyclonal antibody with various affinities to OVA. It is possible that the low LOD is due to the antibody species that have a high affinity to OVA. The use of polyclonal antibodies might have resulted in obtaining a relatively low K_d compared with monoclonal antibodies.[53] On the other hand, the IgG molecule has two identical antigen-binding sites and the distance between the antigen-binding sites is limited. In this work, the density of OVA molecules on the SiNW surface was relatively high; thus, it is possible to establish bivalent interactions with IgG molecules, possibly resulting in an increase of the change in the Gibbs free energy of OVA and IgG binding[54] and increasing its equilibrium constant.[55] Despite the possibility of a relatively high binding affinity between target IgG and OVA, the IgG with low concentrations cannot be detected by a planer FET biosensor because the ratio of the depletion region change to the whole channel was low. We gave sufficient evidence to demonstrate that the sensitivity of the biosensor can be greatly improved by the integration of critical factors for the SiNW biosensor with precise design and fabrication.

At last, a comparison of the performance of SiNW biosensors based on antibody and antigen binding is concluded in Table 1.[29,56−58] Although the detection target biomolecules of the previous studies were different from that of this work, as a reference, the critical factor-integrated SiNW biosensor shows significant improvement of LOD and provides significant potential for rapid, sensitive, and specific diagnosis of diseases at an early stage. In addition, it is also worth paying attention to that by functionalizing specific recognition elements on the SiNW surface, the biosensor can be applied to the detection of viruses, cancer-related biomarkers, nucleic acids, and other disease-related proteins at extremely low concentrations.

4. CONCLUSIONS

To develop a SiNW biosensor with extremely high sensitivity, the detection components of the SiNW biosensor structure, NW functional interface, and target biomolecules were studied and optimized. To improve the sensitivity of the SiNW biosensor sensing mechanism, first, a simple theoretical model was proposed and used to analyze the dependence of several critical factors such as the SiNW type, width, and doping concentration on the resistance change ratio of the SiNW. It was indicated that narrow n-type SiNWs with low impurity doping concentrations are beneficial to detect negatively charged molecules with high sensitivity. Second, based on the theoretical analysis, a SiNW biosensor integrating optimized critical factors was fabricated by a precisely controlled CMOS-compatible process. An n-type Si layer with a doping concentration of 2×10^{16}–6×10^{16} cm^{-3} was fabricated by controlling the phosphorus dopant layer thickness and thermal diffusion temperature. High-quality SiNWs with a width of 16.0 nm were fabricated via a high-resolution EBL process and controllable plasma etching process. The native oxide layer on SiNW was adopted as the gate insulator to transport the captured charged molecules closer to the SiNW surface. As a result of structure optimization, the FET transport behavior of SiNWs with different widths demonstrated that the narrow SiNW channel is beneficial to modulate the channel current by a low gate voltage. The biosensor with the SiNW width of 16 nm shows superior FET characteristics, indicating that the biosensor has significant potential to detect biomolecules at an ultralow concentration. Furthermore, to detect target IgG with high sensitivity and specificity, 2-aminoethylphosphonic acid coupling was employed to modify the surface of the SiNWs and OVA molecules were adopted to functionalize the SiNW surface to capture target IgG molecules. The detection performance of the optimized SiNW biosensor was evaluated by real-time detection of specific IgG molecules at various concentrations and control experiments. The optimized SiNW biosensor revealed ultrahigh sensitivity and high-specificity detection of target IgG with a LOD of 6 aM. The study provides significant potential in applications including detection of viruses, cancer biomarkers, and other proteins

https://dx.doi.org/10.1021/acsami.0c13984
ACS Appl. Mater. Interfaces 2020, 12, 51808−51819

with rapid response, high sensitivity, and high specificity for early disease detection.

■ ASSOCIATED CONTENT

Supporting Information

The Supporting Information is available free of charge at https://pubs.acs.org/doi/10.1021/acsami.0c13984.

FET characteristics of 35 nm and 12 μm wide SiNWs with comparisons to 16 nm wide SiNWs (PDF)

■ AUTHOR INFORMATION

Corresponding Author

Hui Zhang − *Graduate School of Science and Technology, Gunma University, Kiryu, Gunma 376-8515, Japan;* orcid.org/0000-0001-7882-5457; Email: huizhang@gunma-u.ac.jp

Authors

Naoki Kikuchi − *Graduate School of Science and Technology, Gunma University, Kiryu, Gunma 376-8515, Japan*

Noriyasu Ohshima − *Graduate School of Medicine, Gunma University, Maebashi, Gunma 371-8511, Japan*

Taira Kajisa − *Institute of Post-LED Photonics, Tokushima University, Tokushima 770-8506, Japan*

Toshiya Sakata − *Department of Materials Engineering, School of Engineering, The University of Tokyo, Tokyo 113-8656, Japan;* orcid.org/0000-0003-1246-5000

Takashi Izumi − *Graduate School of Medicine, Gunma University, Maebashi, Gunma 371-8511, Japan*

Hayato Sone − *Graduate School of Science and Technology, Gunma University, Kiryu, Gunma 376-8515, Japan*

Complete contact information is available at: https://pubs.acs.org/10.1021/acsami.0c13984

Author Contributions

The manuscript was written through the contribution of all authors. All authors have given approval to the final version of the manuscript.

Notes

The authors declare no competing financial interest.

■ ACKNOWLEDGMENTS

This work was supported by JSPS KAKENHI Grant Nos. 19K23598 (principal investigator, H.Z.), JP18H03547 (principal investigator, H.S.; co-investigators, T.S., H.Z.), and JP26282143 (principal investigator, H.S.; co-investigator, T.S., Sumio Hosaka) and Grants-in-Aid for JSPS Research Fellow No. JP17F17058 (principal investigator, H.S.; co-investigator, H.Z.). We thank the Gunma University Medical Innovation (GUMI) project for providing financial support and Nanotechnology Platform Japan Grant No. JPMXP09F-19-UT-0050 for equipment sharing services.

■ REFERENCES

(1) Corman, V. M.; Landt, O.; Kaiser, M.; Molenkamp, R.; Meijer, A.; Chu, D. K. W.; Bleicker, T.; Brunink, S.; Schneider, J.; Schmidt, M. L.; Mulders, D. G. J. C.; Haagmans, B. L.; Veer, B. V. D.; Brink, S. V. D.; Wijsman, L.; Goderski, G.; Romette, J. L.; Ellis, J.; Zambon, M.; Peiris, M.; Goossens, H.; Reusken, C.; Koopmans, M. P. G.; Drosten, C. Detection of 2019 Novel Coronavirus (2019-nCoV) by Real-time RT-PCR. *Eurosurveillance* **2020**, *25*, 23−30.

(2) Broadhurst, M. J.; Brooks, T. J. G.; Pollock, N. R. Diagnosis of Ebola Virus Disease: Past, Present, and Future. *Clin. Microbiol. Rev.* **2016**, *29*, 773−793.

(3) Xiao, T.; Ying, W.; Li, L.; Hu, Z.; Ma, Y.; Jiao, L.; Ma, J.; Cai, Y.; Lin, D.; Guo, S.; Han, N.; Di, X.; Li, M.; Zhang, D.; Su, K.; Yuan, J.; Zheng, H.; Gao, M.; He, J.; Shi, S.; Li, W.; Xu, N.; Zhang, H.; Liu, Y.; Zhang, K.; Gao, Y.; Qian, X.; Cheng, S. An Approach to Studying Lung Cancer-related Proteins in Human Blood. *Mol. Cell. Proteomics* **2005**, *4*, 1480−1486.

(4) Huang, Y. W.; Wu, C. S.; Chuang, C. K.; Pang, S. T.; Pan, T. M.; Yang, Y. S.; Ko, F. H. Real-Time and Label-Free Detection of the Prostate-Specific Antigen in Human Serum by a Polycrystalline Silicon Nanowire Field-Effect Transistor Biosensor. *Anal. Chem.* **2013**, *85*, 7912−7918.

(5) Fleischhacker, M.; Schmidt, B. Circulating Nucleic Acids (CNAs) and Cancer—A Survey. *Biochim. Biophys. Acta* **2007**, *1775*, 181−232.

(6) Caliendo, A. M.; Gilbert, D. N.; Ginocchio, C. C.; Hanson, K. E.; May, L.; Quinn, T. C.; Tenover, F. C.; Alland, D.; Blaschke, A. J.; Bonomo, R. A.; Carroll, K. C.; Ferraro, M. J.; Hirschhorn, L. R.; Joseph, W. P.; Karchmer, T.; MacIntyre, A. T.; Reller, L. B.; Jackson, A. F. Better Tests, Better Care: Improved Diagnostics for Infectious Diseases. *Clin. Infect Dis.* **2013**, *57*, S139−S170.

(7) Chen, H.; Liu, K.; Li, Z.; Wang, P. Point of Care Testing for Infectious Diseases. *Clin. Chim. Acta* **2019**, *493*, 138−147.

(8) Hijano, D. R.; Cardenas, J. B. D.; Maron, G.; Garner, C. D.; Ferrolino, J. A.; Dallas, R. H.; Gu, Z.; Hayden, R. T. Clinical Correlation of Influenza and Respiratory Syncytial Virus Load Measured by Digital PCR. *PLoS One* **2019**, *14*, No. e0220908.

(9) To, K. K. W.; Tsang, O. T. Y.; Leung, W. S.; Tam, A. R.; Wu, T. C.; Lung, D. C.; Yip, C. C. Y.; Cai, J. P.; Chan, J. M. C.; Chik, T. S. H.; Lau, D. P. L.; Choi, C. Y. C.; Chen, L. L.; Chan, W. M.; Chan, K. H.; Ip, J. D.; Ng, A. C. K.; Poon, R. W. S.; Luo, C. T.; Cheng, V. C. C.; Chan, J. F. W.; Hung, I. F. N.; Chen, Z.; Chen, H.; Yuen, K. Y. Temporal Profiles of Viral Load in Posterior Oropharyngeal Saliva Samples and Serum Antibody Responses During Infection by SARS-CoV-2: An Observational Cohort Study. *Lancet Infect. Dis.* **2020**, *20*, 565−574.

(10) Hermann, N.; Dressen, K.; Schroeder, L.; Debald, M.; Schildberg, F. A.; Bruenagel, G. W.; Hettwer, K.; Uhlig, S.; Kuhn, W.; Hartmann, G.; Holdenrieder, S. Diagnostic Relevance of A Novel Multiplex Immunoassay Panel in Breast Cancer. *Tumor Biol.* **2017**, *39*, 1−11.

(11) Rusling, J. F.; Kumar, C. V.; Gutkind, J. S.; Patel, V. Measurement of Biomarker Proteins for Point-of-care Early Detection and Monitoring of Cancer. *Analyst* **2010**, *135*, 2496−2511.

(12) Castellanos-Gonzalez, A.; White, A. C.; Melby, J. P.; Travi, B. Molecular Diagnosis of Protozoan Parasites by Recombinase Polymerase Amplification. *Acta Trop.* **2018**, *182*, 4−11.

(13) Espy, M. J.; Uhl, J. R.; Sloan, L. M.; Buckwalter, S. P.; Jones, M. F.; Vetter, E. A.; Yao, J. D. C.; Wengenack, N. L.; Rosenblatt, J. E.; Cockerill, F. R.; Smith, T. F. Real-Time PCR in Clinical Microbiology: Applications for Routine Laboratory Testing. *Clin. Microbiol. Rev.* **2006**, *19*, 165−256.

(14) Chen, H.; Wang, H.; Li, X.; You, L.; Wei, J.; Shi, W. Evaluation of a Rapid Detection Influenza Virus a Antigens Kit Using Paired Serum Antibody Test. *Yonsei Med J.* **2013**, *54*, 476−479.

(15) Weinberg, A.; Walker, M. L. Evaluation of Three Immunoassay Kits for Rapid Detection of Influenza Virus A and B. *Clin. Diagn. Lab. Immunol.* **2005**, *12*, 367−370.

(16) https://www.assaygenie.com/covid-19-rapid-poc-test/.

(17) Yang, F.; Zhang, G. J. Silicon Nanowire-transistor Biosensor for Study of Molecule- molecule Interactions. *Rev. Anal. Chem.* **2014**, *33*, 95−110.

(18) Chen, K. I.; Li, B. R.; Chen, Y. T. Silicon Nanowire Field-effect Transistor-based Biosensors for Biomedical Diagnosis and Cellular Recording Investigation. *Nano Today* **2011**, *6*, 131−154.

(19) Cui, Y.; Wei, Q. Q.; Park, H. K.; Lieber, C. M. Nanowire Nanosensors for Highly Sensitive and Selective Detection of Biological and Chemical Species. *Science* **2001**, *293*, 1289−1292.
(20) Zhang, G. J.; Ning, Y. Silicon Nanowire Biosensor and Its Applications in Disease Diagnostics: A Review. *Anal. Chim. Acta* **2012**, *749*, 1−15.
(21) Namdari, P.; Daraee, H.; Eatemadi, A. Recent Advances in Silicon Nanowire Biosensors: Synthesis Methods, Properties, and Applications. *Nanoscale Res. Lett.* **2016**, *11*, No. 406.
(22) Zhang, Y. L.; Chen, R. M.; Xu, L.; Ning, Y.; Xie, S. G.; Zhang, G. J. Silicon Nanowire Biosensor for Highly Sensitive and Multiplexed Detection of Oral Squamous Cell Carcinoma Biomarkers in Saliva. *Anal. Sci.* **2015**, *31*, 73−78.
(23) Ahmad, R.; Mahmoudi, T.; Ahn, M. S.; Hahn, Y. B. Recent Advances in Nanowires-based Field-effect Transistors for Biological Sensor Applications. *Biosens. Bioelectron.* **2018**, *100*, 312−325.
(24) He, J.; Zhu, J.; Gong, C.; Qi, J.; Xiao, H.; Jiang, B.; Zhao, Y. Label-Free Direct Detection of miRNAs with Poly-Silicon Nanowire Biosensors. *Plos One* **2015**, *10*, No. e0145160.
(25) Uhm, M.; Lee, J.-M.; Lee, J.; Lee, J. H.; Choi, S.; Park, B.-G.; Kim, D. M.; Choi, S.-J.; Mo, H.-S.; Jeong, Y.-J.; Kim, D. H. Ultrasensitive Electrical Detection of Hemagglutinin for Point-of-Care Detection of Influenza Virus Based on a CMP-NANA Probe and Top-Down Processed Silicon Nanowire Field-Effect Transistors. *Sensors* **2019**, *19*, No. 4502.
(26) Sakata, T.; Matsuse, Y. In Situ Electrical Monitoring of Cancer Cells Invading Vascular Endothelial Cells with Semiconductor-Based Biosensor. *Genes Cells* **2017**, *22*, 203−209.
(27) Sakata, T. Biologically Coupled Gate Field-Effect Transistors Meet in Vitro Diagnostics. *ACS Omega* **2019**, *4*, 11852−11862.
(28) Nuzaihan M. N, M.; Hashim, U.; Arshad, M. K. M.; Ruslinda, A. R.; Rahman, S. F. A.; Fathil, M. F. M.; Ismail, M. H. Top-Down Nanofabrication and Characterization of 20 nm Silicon Nanowires for Biosensing Applications. *PLoS One* **2016**, *11*, No. e0152318.
(29) Kim, A.; Ah, C. S.; Yu, H. Y.; Yang, J. H.; Baek, I. B.; Ahn, C. G.; Park, C. W.; Jun, M. S.; Lee, S. Ultrasensitive, Label-free, and Real-time Immunodetection Using Silicon Field-effect Transistors. *Appl. Phys. Lett.* **2007**, *91*, No. 103901.
(30) Chua, J. H.; Chee, R. E.; Agarwal, A.; Wong, S. M.; Zhang, G. J. Label-free Electrical Detection of Cardiac Biomarker with Complementary Metal-Oxide Semiconductor-Compatible Silicon Nanowire Sensor Arrays. *Anal. Chem.* **2009**, *81*, 6266−6271.
(31) Gao, A.; Lu, N.; Wang, Y.; Dai, P.; Li, T.; Gao, X.; Wang, Y.; Fan, C. Enhanced Sensing of Nucleic Acids with Silicon Nanowire Field Effect Transistor Biosensors. *Nano Lett.* **2012**, *12*, 5262−5268.
(32) Tran, D. P.; Pham, T. T. T.; Wolfrum, B.; Offenhausser, A.; Thierry, B. CMOS-Compatible Silicon Nanowire Field-Effect Transistor Biosensor: Technology Development toward Commercialization. *Materials* **2018**, *11*, No. 785.
(33) Ohno, Y.; Maehashi, K.; Matsumoto, K. Label-free Biosensors based on Aptamer-Modified Graphene Field-Effect Transistors. *J. Am. Chem. Soc.* **2010**, *132*, 18012−18013.
(34) Maehashi, K.; Ohno, Y.; Matsumoto, K. Utilizing Research into Electrical Double Layers as A Basis for The Development of Label-free Biosensors Based on Nanomaterial Transistors Nanobiosensors in. *Dis. Diagn.* **2016**, *5*, 1−13.
(35) Choi, J.; Ide, A.; Truong, Y. B.; Kyratzis, I. L.; Caruso, R. A. High Surface Area Mesoporous Titanium−zirconium Oxide Nanofibrous Web: A Heavy Metal Ion Adsorbent. *J. Mater. Chem. A* **2013**, *1*, 5847−5853.
(36) Das, M.; Mishra, D.; Maiti, T. K.; Basak, A.; Pramanik, P. Biofunctionalization of Magnetite Nanoparticles Using an Aminophosphonic Acid Coupling Agent: New, Ultradispersed, Iron-Oxide Folate Nanoconjugates for Cancer-Specific Targeting. *Nanotechnology* **2008**, *19*, No. 415101.
(37) Sakata, T.; Kamahori, M.; Miyahara, Y. DNA analysis chip based on field-effect transistors. *Jpn. J. Appl. Phys.* **2005**, *44*, 2854−2859.
(38) Xie, P.; Hu, Y.; Fang, Y.; Huang, J.; Lieber, C. M. Diameter-dependent Dopant Location in Silicon and Germanium Nanowires. *Proc. Natl. Acad. Sci. U.S.A.* **2009**, *106*, 15254−15258.
(39) Irvin, J. C. Resistivity of Bulk Silicon and of Diffused Layers in Silicon. *Bell Syst. Tech. J.* **1962**, *41*, 387.
(40) Zhang, H.; Hosaka, S.; Yin, Y. Ordering of Self-assembled 5-nm-diameter Poly(dimethylsiloxane) Nanodots with Sub-10 nm Pitch Using Ultra-narrow Electron-beam-drawn Guide Lines and Three-dimensional Control. *Appl. Phys. Lett.* **2014**, *104*, No. 093107.
(41) Komori, T.; Zhang, H.; Akahane, T.; Mohamad, Z.; Yin, Y.; Hosaka, S. Electron Beam Lithography of 15 × 15 nm2 Pitched Nanodot Arrays with a Size of Less than 10 nm Using High Development Contrast Salty Developer. *Jpn. J. Appl. Phys.* **2012**, *51*, No. 06FB02.
(42) Zhang, H.; Huda, M.; Komori, T.; Zhang, Y.; Yin, Y.; Hosaka, S. Estimation of Pattern Resolution Using NaCl high-contrast Developer by Monte Carlo Simulation of Electron Beam Lithography. *Microelectron. Eng.* **2014**, *121*, 142−146.
(43) Tomoya, T.; Zhang, H.; Oshima, K.; Sakurai, Y.; Suzuki, T.; Ohshima, N.; Izumi, T.; Sone, H. Fabrication of N-Type Silicon Nanowire Biosensor for Sub-10-Femtomolar Concentration of Immunoglobulin. *Key Eng. Mater.* **2018**, *790*, 28−33.
(44) Schwartz, J.; Avaltroni, M. J.; Danahy, M. P.; Silverman, B. M.; Hanson, H.L.; Schwarzbauer, J. E.; Midwood, K. S.; Gawalt, E. S. Cell Attachment and Spreading on Metal Implant Materials. *Mater. Sci. Eng., C* **2003**, *23*, 395−400.
(45) Midwood, K. S.; Carolus, M. D.; Danahy, M. P.; Schwarzbauer, J. E.; Schwartz, J. Easy and Efficient Bonding of Biomolecules to an Oxide Surface of Silicon. *Langmuir* **2004**, *20*, 5501−5505.
(46) Tan, Y. H.; Liu, M.; Nolting, B.; Go, J. G.; Hague, J. G.; Liu, G. Nanoengineering Approach for Investigation and Regulation of Protein Immobilization. *ACS Nano* **2008**, *2*, 2374−2384.
(47) Matsumoto, T.; Inoue, H. Overall Structure, and Surface Roughness of Native Ovalbumin Molecules in Aqueous Solutions at Various Ionic Concentrations. *J. Colloid Interface Sci.* **1993**, *160*, 105−109.
(48) de Moraes, A.; Kubota, L. T. Recent Trends in Field-Effect Transistors-Based Immunosensors. *Chemosensors* **2016**, *4*, No. 20.
(49) Saha, B.; Evers, T. H.; Prins, M. W. J. How Antibody Surface Coverage on Nanoparticles Determines the Activity and Kinetics of Antigen Capturing for Biosensing. *Anal. Chem.* **2014**, *86*, 8158−8166.
(50) Hill, A. V. A New Mathematical Treatment of Changes of Ionic Concentration in Muscle and Nerve under The Action of Electric Currents, with a Theory as to Their Mode of Excitation. *J. Physiol.* **1910**, *40*, 190−224.
(51) Kajisa, T.; Li, W.; Michinobu, T.; Sakata, T. Well-designed Dopamine-Imprinted Polymer Interface for Selective and Quantitative Dopamine Detection Among Catecholamines Using a Potentiometric Biosensor. *Biosens. Bioelectron.* **2018**, *117*, 810−817.
(52) Masuda, T.; Yasumoto, K.; Kitabatake, N. Monitoring the Irradiation-induced Conformational Changes of Ovalbumin by Using Monoclonal Antibodies and Surface Plasmon Resonance. *Biosci., Biotechnol., Biochem.* **2000**, *64*, 710−716.
(53) Ascoli, C. A.; Aggeler, B. Overlooked Benefits of Using Polyclonal Antibodies. *BioTechniques* **2018**, *65*, 127−136.
(54) Hadzhieva, M.; Pashov, A. D.; Kaveri, S.; Desmazes, S. L.; Mouquet, H.; Dimitrov, J. D. Impact of Antigen Density on the Binding Mechanism of IgG Antibodies. *Sci. Rep.* **2017**, *7*, No. 3767.
(55) Reverberi, R.; Reverberi, L. Factors Affecting the Antigen-antibody Reaction. *Blood Transfus.* **2007**, *5*, 227−240.
(56) Regonda, S.; Tian, R.; Gao, J.; Greene, S.; Ding, J.; Hu, W. Silicon Multi-nanochannel FETs to Improve Device Uniformity/stability and Femtomolar Detection of Insulin in Serum. *Biosens. Bioelectron.* **2013**, *45*, 245−251.
(57) Puppo, F.; Doucey, M.-A.; Delaloye, J.-F.; Moh, T. S. Y.; Pandraud, G.; Sarro, P. M.; Micheli, G. D.; Carrara, S. Femto-molar Sensitive Field Effect Transistor Biosensors based on Silicon Nanowires and Antibodies. *IEEE Sens.* **2014**, *13977879*, 866.

https://dx.doi.org/10.1021/acsami.0c13984
ACS Appl. Mater. Interfaces 2020, 12, 51808−51819

(58) Zheng, G.; Patolsky, F.; Cui, Y.; Wang, W. U.; Lieber, C. M. Multiplexed Electrical Detection of Cancer Markers with Nanowire Sensor Arrays. *Nat. Biotechnol.* **2005**, *23*, 1294−1301.

https://dx.doi.org/10.1021/acsami.0c13984
ACS Appl. Mater. Interfaces 2020, 12, 51808−51819